

## THE INFRARED EMISSION AND OPENING ANGLE OF THE TORUS IN QUASARS

MING-YANG ZHUANG,<sup>1,2</sup> LUIS C. HO,<sup>1,2</sup> AND JINYI SHANGGUAN<sup>1,2</sup>

<sup>1</sup>*Kavli Institute for Astronomy and Astrophysics, Peking University, Beijing 100871, China*

<sup>2</sup>*Department of Astronomy, School of Physics, Peking University, Beijing 100871, China*

### ABSTRACT

According to the unified model of active galactic nuclei (AGNs), a putative dusty torus plays an important role in determining their external appearance. However, very limited information is known about the physical properties of the torus. We perform detailed decomposition of the infrared ( $1 - 500 \mu\text{m}$ ) spectral energy distribution of 76  $z < 0.5$  Palomar-Green quasars, combining photometric data from 2MASS, *WISE*, and *Herschel* with *Spitzer* spectroscopy. Our fits favor recent torus spectral models that properly treat the different sublimation temperatures of silicates and graphite and consider a polar wind component. The AGN-heated dust emission from the torus contributes a significant fraction ( $\sim 70\%$ ) of the total infrared ( $1 - 1000 \mu\text{m}$ ) luminosity. The torus luminosity correlates well with the strength of the ultraviolet/optical continuum and the broad H $\beta$  emission line, indicating a close link between the central ionization source and re-radiation by the torus. Consistent with the unified model, most quasars have tori that are only mildly inclined along the line-of-sight. The half-opening angle of the torus, a measure of its covering factor, declines with increasing accretion rate until the Eddington ratio reaches  $\sim 0.5$ , above which the trend reverses. This behavior likely results from the change of the geometry of the accretion flow, from a standard geometrically thin disk at moderate accretion rates to a slim disk at high accretion rates.

*Keywords:* galaxies: active — galaxies: nuclei — galaxies: quasars: general — infrared: general — accretion, accretion disks

## 1. INTRODUCTION

Active galactic nuclei (AGNs) release prodigious amounts of energy from accretion of matter by massive black holes (BHs) residing in the center of galaxies (Lynden-Bell 1969; Rees 1984). Many attempts have been made to explain the tremendous observed diversity of AGNs through “unified” models (Antonucci 1993; Urry & Padovani 1995; Netzer 2015). In these models, a small-scale ( $\lesssim 1$  pc) dusty torus plays an important role in separating type 1 and type 2 AGNs by reprocessing the ultraviolet, optical, and X-ray radiation into the infrared (IR) band, and by blocking photons from the broad-line region from certain viewing angles.

Early mid-IR observations with the Very Large Telescope Interferometer by Tristram et al. (2007) provided strong evidence supporting the existence of a clumpy-structured torus (e.g., Krolik & Begelman 1988; Dullemond & van Bemmelen 2005) rather than a smooth torus (e.g., Pier & Krolik 1992; Efstathiou & Rowan-Robinson 1995). Intensive efforts have been invested to model the emission from the torus (Hönig et al. 2006; Schartmann et al. 2008; Nenkova et al. 2008b,a; Hönig et al. 2010; Stalevski et al. 2012; Siebenmorgen et al. 2015). These models have been extensively employed to investigate the torus covering factor and intrinsic differences between type 1 and type 2 AGNs (e.g., Alonso-Herrero et al. 2011; Stalevski et al. 2016; Ezhikode et al. 2017). The covering factor of the torus can also be constrained using gas column densities probed by X-ray observations (e.g., Ueda et al. 2007; Brightman & Ueda 2012). Ricci et al. (2017) report that the torus covering factor is linked with the Eddington ratio of the BH.

Subsequent interferometric observations (Raban et al. 2009; Hönig et al. 2013; López-Gonzaga et al. 2014; López-Gonzaga & Jaffe 2016) reveal that the bulk of the mid-IR emission of AGNs actually arises from a polar-extended component, which dominates the energy output in that band, while the near-IR emission still emanates from a classical, small-scale disk-like component. This discovery radically alters the traditional view of a single torus structure and demands an update of the present torus models. Moreover, detailed scrutiny of the spectral energy distribution (SED) of AGNs (Deo et al. 2011; Mor & Netzer 2012) consistently finds that an extra, high-temperature blackbody component is needed to account for the near-IR emission in type 1 AGNs, indicating the existence of hot graphite grains not fully represented in current models of clumpy tori (e.g., Nenkova et al. 2008a,b; Hönig et al. 2010; Siebenmorgen et al. 2015). This shortcoming has been addressed recently by García-González et al. (2017), who incorporated more physical dust sublima-

tion temperatures for silicates and graphite into their torus models. Hönig & Kishimoto (2017) further added a polar wind component to mimic the structures seen in the latest interferometric observations.

We apply these newly developed models to investigate the physical properties of the torus in a large sample of low-redshift quasars, using the comprehensive set of high-quality IR SEDs spanning  $\sim 1 - 500 \mu\text{m}$  assembled by Shangguan et al. (2018). The SEDs combine both photometric data and mid-IR spectroscopy. We use our recently developed Bayesian Markov Chain Monte Carlo (MCMC) method to decompose the SEDs into their main constituent components, paying special emphasis on evaluating the performance of the latest spectral templates for the AGN torus. We quantify the fractional contribution of the torus luminosity to the total IR energy budget and study the inclination angle and covering factor of the torus.

This paper is structured as follows. We introduce the torus models used in this paper in Section 2. We show the results of the SED fitting in Section 3 and discuss the properties of the torus in Section 4. Conclusions are presented in Section 5. This work adopts the following parameters for a  $\Lambda$ CDM cosmology:  $\Omega_m = 0.308$ ,  $\Omega_\Lambda = 0.692$ , and  $H_0 = 67.8 \text{ km s}^{-1} \text{ Mpc}^{-1}$  (Planck Collaboration et al. 2016).

## 2. MODELS

We use up to four components to fit the IR SED (Figure 1): (1) host galaxy stellar emission peaking in the near-IR, (2) AGN torus emission peaking in the near-IR and mid-IR, (3) cold dust emission from the large-scale interstellar medium of the host galaxy peaking in the far-IR, and, if necessary, (4) an extra synchrotron jet component in the case of radio-loud objects. We adopt the same models as Shangguan et al. (2018) for the stellar emission (Bruzual & Charlot 2003; BC03), interstellar dust emission (Draine & Li 2007; DL07), and synchrotron radiation (Pe’er 2014; broken power-law). For the torus emission, apart from the CLUMPY model (Nenkova et al. 2008a,b) and the complementary blackbody component (BB) added to account for emission from very hot dust as employed by Shangguan et al. (2018), here we make use of two sets of newly calculated torus models (“Clumpy AGN Tori in a 3D geometry”, CAT3D, Hönig et al. 2010) recently developed by García-González et al. (2017) and Hönig & Kishimoto (2017).

Nenkova et al. (2008a,b) developed a formalism to perform radiative transfer calculations of clumpy clouds in a torus, which enables a large range of dust temperatures to coexist at the same distance from the central

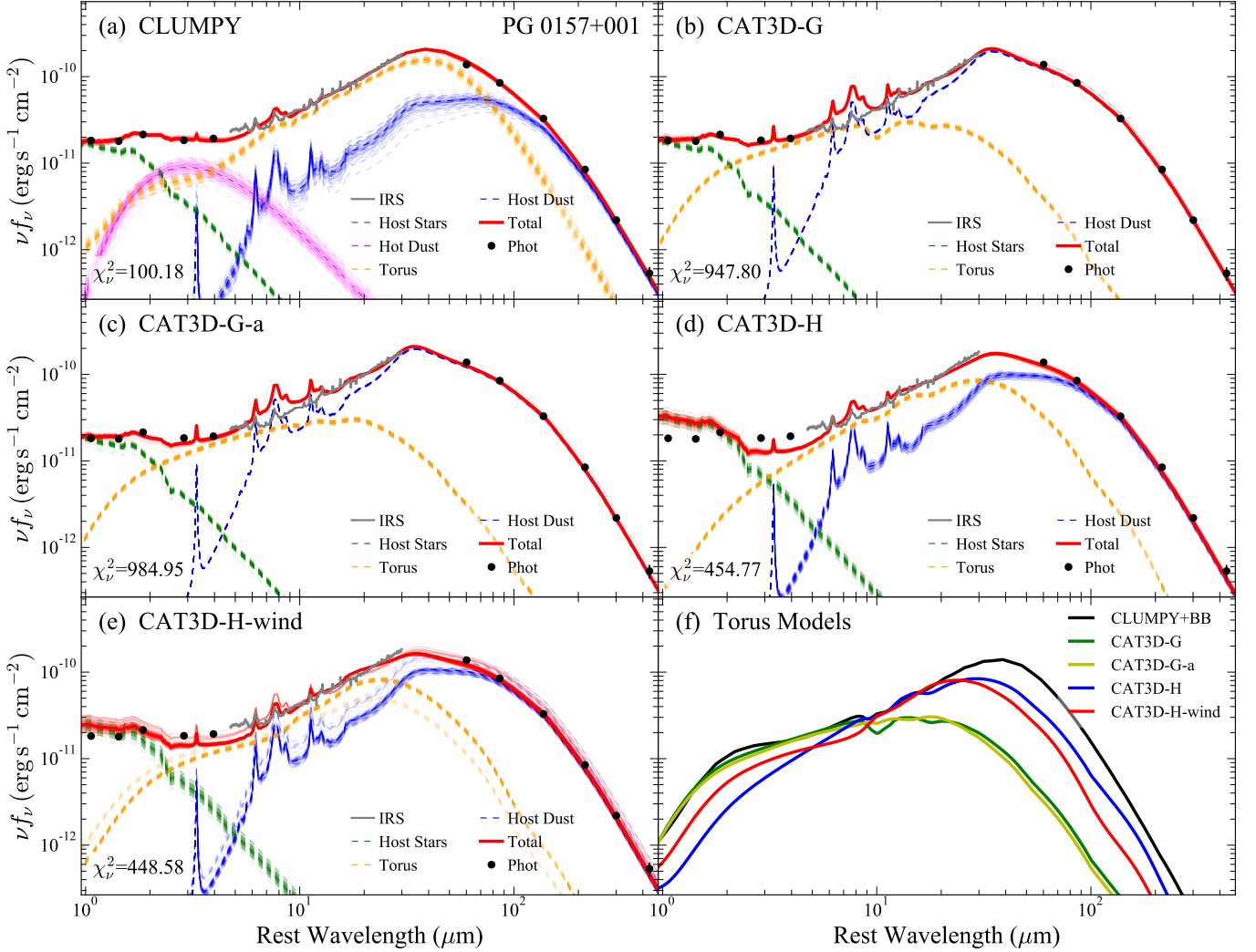


**Figure 1.** Examples of SED fitting for PG 0157+001, employing torus models from (a) CLUMPY, (b) CAT3D-G, (c) CAT3D-G-a, (d) CAT3D-H, and (e) CAT3D-H-wind. Panel (f) compares the torus components of all five torus models. In panels (a)–(e), the grey line represents the *Spitzer*/IRS spectrum, and the black points show photometric data from 2MASS, *WISE*, and *Herschel*. The dashed lines are the best-fit models: host galaxy stars (BC03; green), torus (orange), and host galaxy dust (DL07; blue). In the case of panel (a), the CLUMPY torus model is supplemented with an additional blackbody component for very hot dust (magenta). The combined, best-fit total model is the red solid line. To visualize the model uncertainties, the associated thin lines in light color represent 100 sets of models with parameters drawn randomly from the space sampled by the MCMC algorithm. The reduced chi-squared ( $\chi^2_\nu$ ) for the part of the SED covering the IRS spectrum is shown on the lower-left corner of panels (a)–(e) to quantify the goodness-of-fit (see Appendix B for details). The complete figure set (76 figures) of fitting results with CAT3D-H-wind torus model is available in the online journal.

radiation source. They assume a sublimation temperature of  $\sim 1500$  K for both silicate and graphite dust. Their model has seven free parameters to characterize the properties of the torus: (1) the optical depth  $\tau_V$  of individual clouds, (2) the power-law index  $q$  of the radial distribution of clouds, (3) the ratio  $Y$  between the outer and inner sublimation radius  $r_{\text{sub}}$ , (4) the average number of clouds in the equatorial direction  $N_0$ , (5) the standard deviation  $\sigma$  of the Gaussian distribution of the number of clouds in the vertical direction, (6) the observer’s viewing angle  $i$  with respect to the normal of

the torus plane, and (7) a normalization factor  $L$ . Together with two additional free parameters for the BB to account for the very hot dust component, there are a total of nine free parameters. The CLUMPY model has more than 1.2 million spectral templates, covering a large range of parameter space.

Building upon the original framework of the torus model of Hönig et al. (2010), Hönig & Kishimoto (2017) expanded the CAT3D model to account for the mid-IR observational evidence of extended dust emission emanating from the polar direction of the nuclear regions

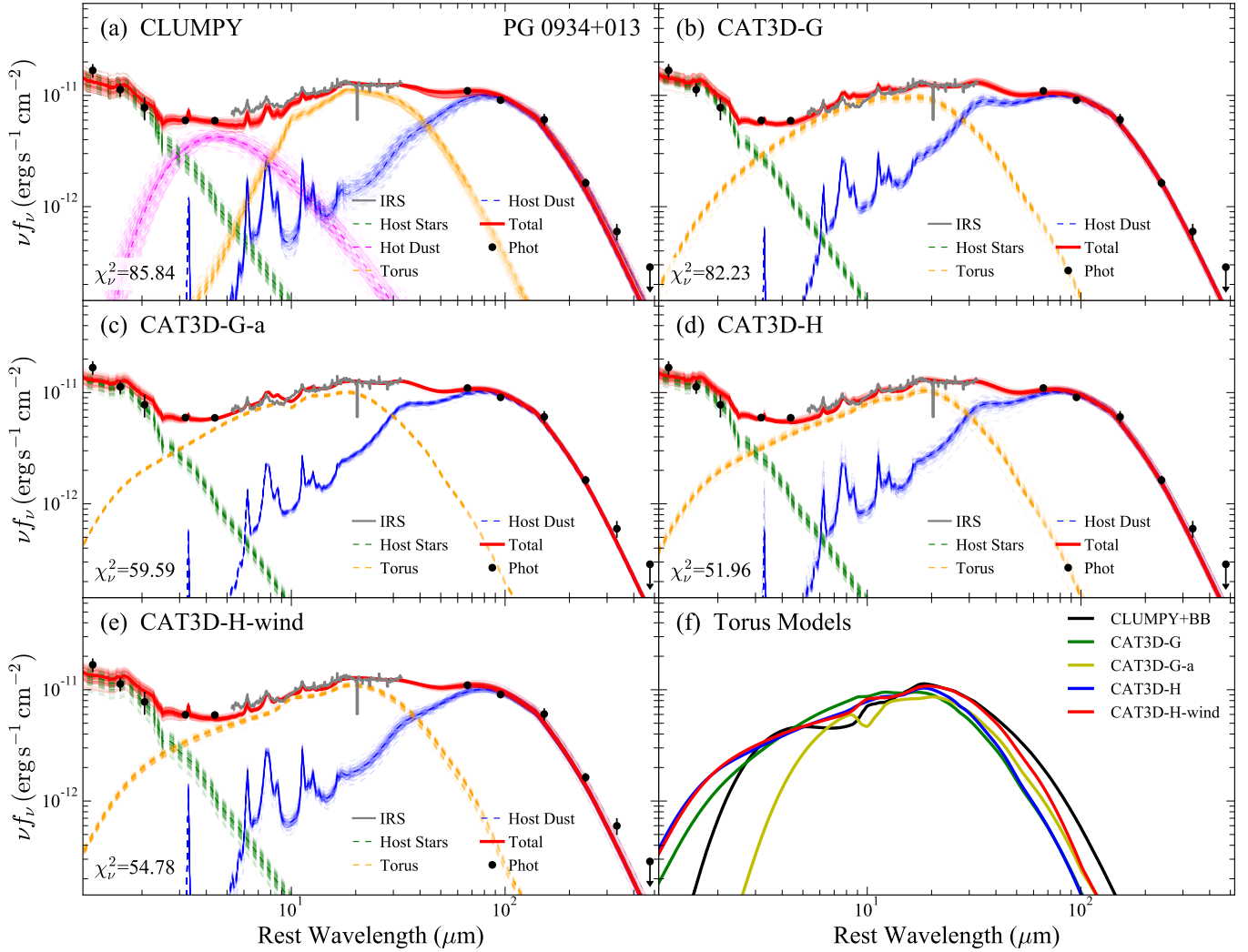


**Figure 2.** Same as Figure 1, but for PG 0934+013.

of AGNs (Raban et al. 2009; Hönig et al. 2013; López-Gonzaga et al. 2014; López-Gonzaga & Jaffe 2016), and to allow for the possibility that silicates and graphite have different sublimation temperatures and grain size distributions. While silicates sublimate at temperatures higher than  $\sim 1200$  K, graphite can withstand temperatures up to  $\sim 1900$  K (e.g., Barvainis 1987; Kishimoto et al. 2007; Mor & Netzer 2012; Hönig & Kishimoto 2017). Supposing that the extended nuclear dust arises from some kind of outflow, they consider a wind component with the shape of a hollow cone in the polar region of the AGN, possibly formed by dust clouds lifted by radiation pressure near the dust sublimation radius. Three free parameters specify the properties of the torus properties: the power-law index  $a$  of the cloud radial distribution of the form  $r^a$ , with  $r$  the distance from the center in units of  $r_{\text{sub}}$ ; the dimensionless scale height  $h$  of the Gaussian distribution of clouds in the vertical

direction of the form  $\exp\{-z^2/2(hr)^2\}$ , with  $z$  the vertical distance distribution from the mid-plane; and the average number  $N_0$  of clouds along the equatorial line-of-sight. The wind itself is characterized by five free parameters: the radial distribution  $a_w$  of dust clouds, the half-opening angle  $\theta_w$ , the angular width  $\sigma_\theta$ , and a wind-to-disk ratio  $f_{\text{wd}}$ , which defines the ratio between the number of clouds along the cone and  $N_0$ . Together with the inclination (i.e. viewing) angle  $i$  and normalization factor  $\log L$ , there are nine free parameters in total. The model holds constant three additional parameters, namely the outer radius of the torus and wind  $R_{\text{out}}$ , the size of each cloud  $R_{\text{cl}}$ , and the optical depth of each cloud  $\tau_V$ . Two sets of torus models are provided, with (CAT3D-H-wind) and without (CAT3D-H) winds. Both cases properly treat the size distribution and dust sublimation temperature for silicates and graphite grains. The parameter space for the two sets of models is dif-



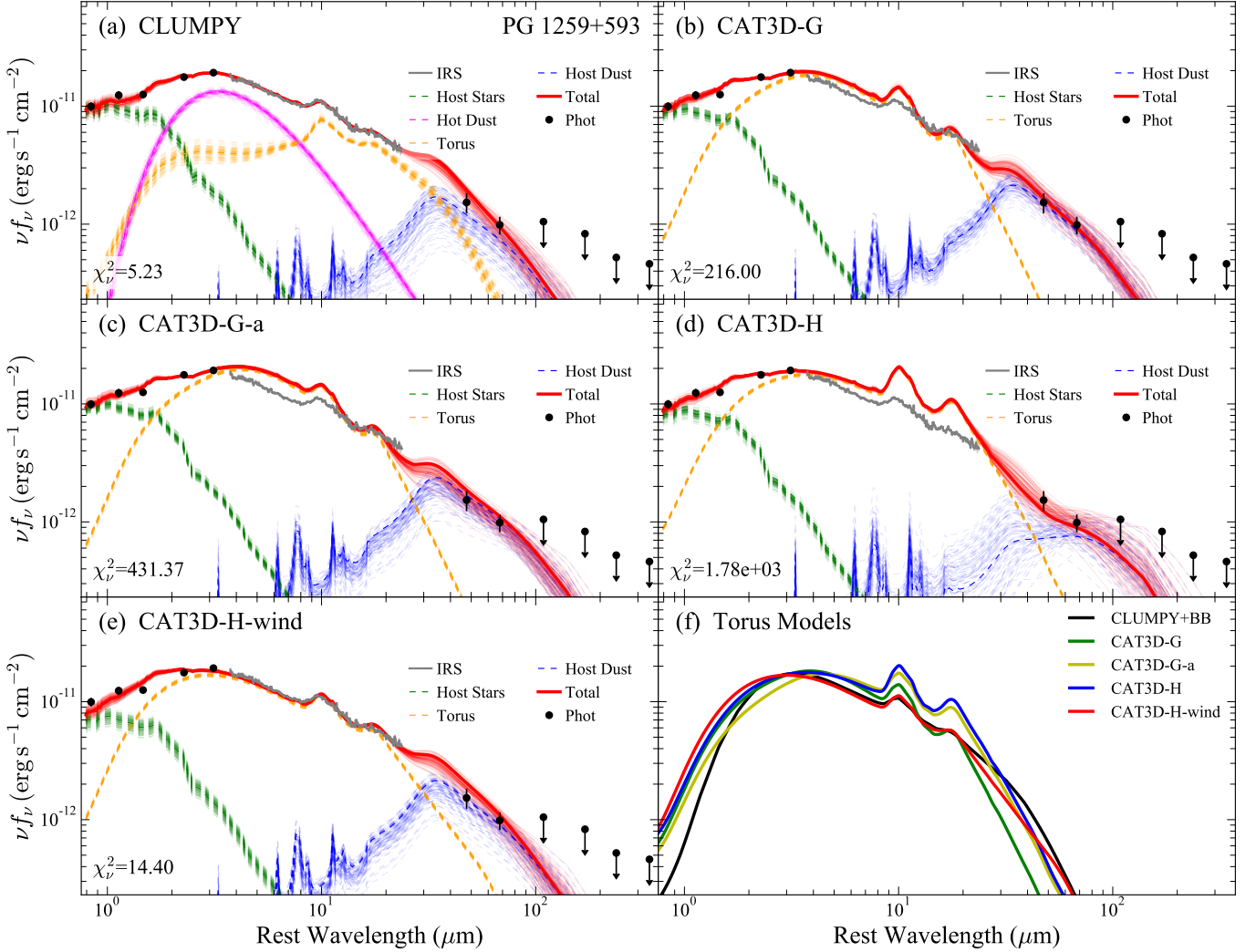


**Figure 3.** Same as Figure 1, but for PG 1259+593.

ferent, and the number of spectral templates is also different. Hönic & Kishimoto (2017) provide 132,300 templates for CAT3D-H-wind and 1,078 templates for CAT3D-H.

Similar to Hönic & Kishimoto (2017), García-González et al. (2017) improved the original CAT3D model with a more realistic physical treatment of differential dust grain sublimation and anisotropic AGN emission, motivated by the expectation that the ultraviolet photons produced by the accretion disk are angularly dependent ( $\cos i$ ). Again, two sets of torus models are available. One considers only the effects of different sublimation temperatures (CAT3D-G), and the other includes, in addition, anisotropic AGN emission (CAT3D-G-a). Both sets of models have the same free parameters but cover a different range of values: power-law index of cloud radial distribution  $a$ , half-opening angle  $\theta_0$ , number of clouds along equatorial direction

$N_0$ , inclination angle  $i$ , and normalization factor  $L$ . The optical depth  $\tau_V$  and outer radius of the torus  $R_{\text{out}}$  are kept fixed. The CAT3D-G model contains 1,232 templates, each with 10 random distributions of clouds; the CAT3D-G-a model only covers 427 templates with each having 20 random distributions of clouds (García-González et al. 2017).

### 3. RESULTS

Our analysis is based on the database of Shangguan et al. (2018), who presented complete IR ( $\sim 1 - 500 \mu\text{m}$ ) SEDs of a sample of 87 low-redshift ( $z < 0.5$ ) type 1 (broad-lined) quasars selected by Boroson & Green (1992) from the Palomar-Green (PG) survey (Schmidt & Green 1983). The SEDs were assembled using photometric data acquired from the Two Micron All-Sky Survey (2MASS), *Wide-field Infrared Survey Explorer* (WISE), and *Herschel Space Observatory* (Herschel), in concert with low-resolution mid-IR spectra taken with

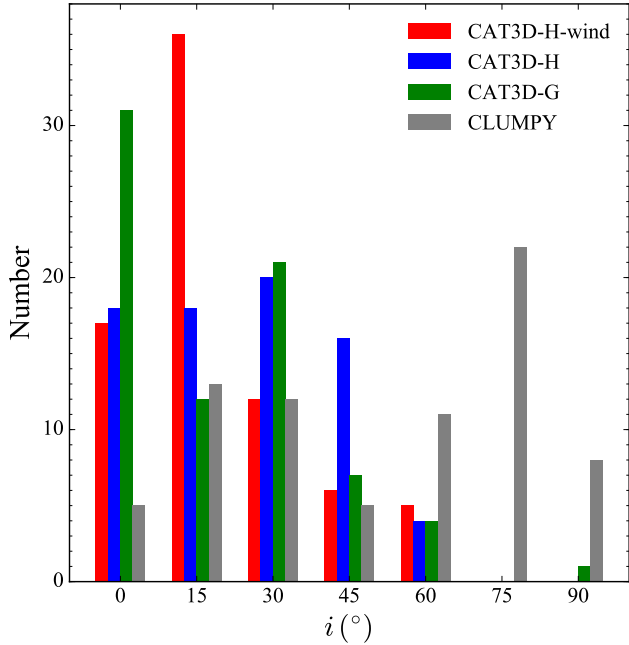


**Figure 4.** Inclination angle ( $i$ ) of the torus derived from different models: CAT3D-H-wind (red), CAT3D-H (blue), CAT3D-G (green), and CLUMPY (gray). The distributions of  $i$  derived from the three CAT3D models are similar and favor low values. By contrast, the CLUMPY model gives a much broader distribution of  $i$ , with a significant fraction of  $i$  larger than  $60^\circ$ .

the Infrared Spectrometer (IRS) on the *Spitzer Space Telescope* (*Spitzer*). Excluding 11 objects with insufficient far-IR detections from *Herschel*, our final sample consists of 76 PG quasars.

We fit the SEDs using the method newly developed by Shangguan et al. (2018). Physical models of host galaxy starlight, AGN torus, and galaxy-scale cold dust are combined to fit the integrated quasar SED using an MCMC method. The photometric and spectroscopic data are fit simultaneously, incorporating both detections and upper limits. The mid-IR photometry, being redundant with the IRS spectra, has a negligible effect on the likelihood; we mitigate this effect by modeling the covariance of the residuals between the spectrum and the model. Five sets of models are applied, corresponding to each of the five different sets of torus templates (CLUMPY+BB and the four versions of CAT3D). For the models of García-González et al. (2017), we use the first of 10 random sets of CAT3D-G templates, and the median value of 20 random sets of CAT3D-G-a templates as the final template for each configuration. Following Shangguan et al. (2018), we choose a 5 Gyr stellar population with a Chabrier (2003) initial mass function from BC03 for the starlight component, and we em-

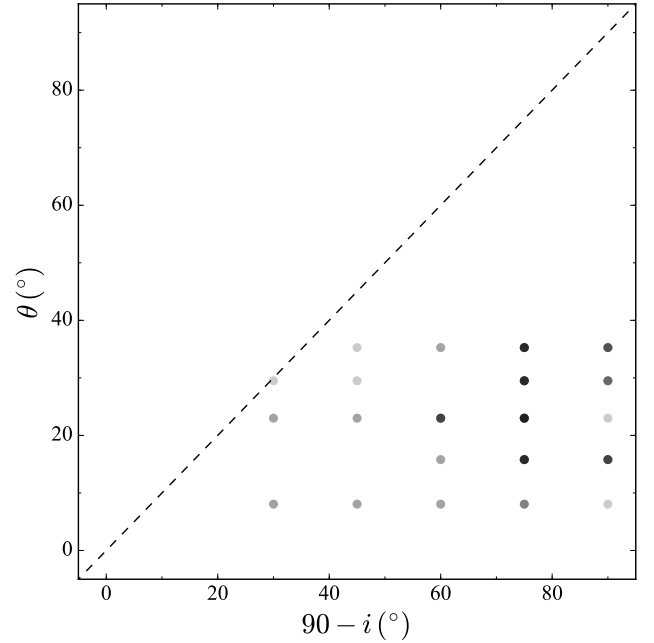


**Figure 5.** Comparison of the torus inclination angle  $i$  (complementary angle  $90^\circ - i$ ) and half-opening angle  $\theta$  from the CAT3D-H-wind model. The dashed line is the 1:1 relation. Because of the discreteness of the parameter space, we do not show error bars. Darker points indicate more objects.

ploy emission templates from DL07 for the host galaxy dust component<sup>1</sup>. For 11 radio-loud objects, we incorporate a synchrotron emission component for the jet, fitting the SED with archival radio measurements collected in Shangguan et al. (2018). However, the synchrotron emission is not dominant at sub-millimeter wavelengths for any of the objects.

### 3.1. Fitting Results

Among the five torus models, CAT3D-H-wind, which incorporates a polar wind component, and CLUMPY provide excellent overall fits to almost all the objects. The other three CAT3D models produce good fits for less than half of the sample. A quantitative assessment is given in Appendix B. Three examples are given in Figures 1–3, which show fits using all five torus models, together with a direct comparison of the best-fit torus components. In the case of PG 1259+593 (Figure 3), which has prominent silicate emission at  $\sim 10 \mu\text{m}$  and very strong hot dust emission at  $\sim 5 \mu\text{m}$ , the new torus models that lack a wind component (CAT3D-G, CAT3D-G-a, CAT3D-H) clearly perform poorly. With-

<sup>1</sup> For completeness, we note that the choice of torus model adopted for the SED fit makes very little difference on the derived dust masses. This is quantified in Appendix A.

out an additional polar wind component, these three models always predict much stronger silicate emission. This is likely because for torus models with only a toroidal structure, the distribution of silicates is directly tied to that of graphite, such that stronger hot dust emission always leads to stronger silicate emission (see Appendix B for details). By contrast, the CAT3D-H-wind model matches closely the overall SED. This strongly suggests that PG 1259+593 indeed has a dusty polar wind. As discussed in Hönig & Kishimoto (2017), the wind component dominates the mid-IR emission while the torus itself is responsible for the hot near-IR emission (Hönig et al. 2013). The near-IR emission and the bulk of the mid-IR emission are isolated naturally, obviating the need to have such strong silicate emission. Not surprisingly, the CLUMPY model, when combined with an extra hot BB component, has the flexibility to give an equally good fit. However, the ad hoc nature of the hot BB component renders this option less desirable. The CAT3D-G-a model generally performs most poorly, possibly because of the limited number of available spectral templates; we do not consider this model further in the following analysis.

### 3.2. Inclination Angle $i$ and Half-opening Angle $\theta$

As our sample consists of type 1 quasars, their broad-line region is directly visible to us. This generally restricts the inclination angle along the line-of-sight  $i$  to be relatively low. Furthermore, the torus should not block the photons from the broad-line region, which means that the complementary angle of the inclination ( $90^\circ - i$ ) should be larger than the half-opening angle  $\theta$ , although there is still a chance for us to see the broad-line region at large inclination because of the clumpy structure of the torus (Nenkova et al. 2008a). According to the definition of the scale height  $h$  for the CAT3D-H and CAT3D-H-wind scenarios,  $\theta = \sqrt{2} \arctan h$ .

Figure 4 shows the values of  $i$  derived from the four torus models. All of the three variants of the CAT3D templates deliver inclination angles clustered toward relatively low values (mostly  $i \lesssim 45^\circ$ ), consistent with expectations. By contrast, the CLUMPY (plus BB) model, despite its success in reproducing the overall SED, yields a very broad distribution of inclinations, with more than half of the sample having  $i \gtrsim 60^\circ$ . Such large inclinations are inconsistent with the type 1 nature of these sources. Apart from the unrealistically large values of  $i$ , the CLUMPY model, as previously mentioned, needs to be supplemented with an extra, artificially added blackbody component to compensate for the lack of emission from hot dust at  $\sim 5 \mu\text{m}$  (Deo et al. 2011; Mor & Netzer 2012). This would result in a mis-

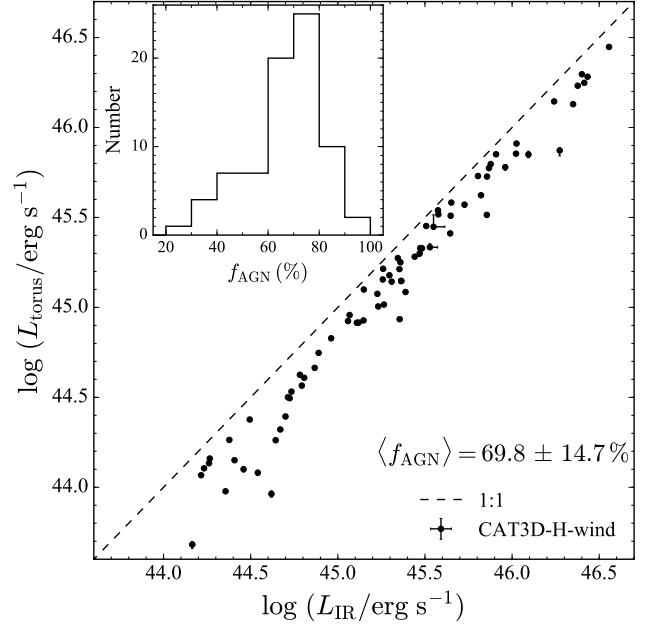


**Figure 6.** Relation between total IR (1–1000  $\mu\text{m}$ ) luminosity ( $L_{\text{IR}}$ ) and the luminosity of the torus ( $L_{\text{torus}}$ ) derived from fits using the CAT3D-H-wind model. Error bars represent the 68% confidence interval determined from the 16th and 84th percentile of the marginalized posterior probability density function; most error bars are smaller than the size of the symbols. The median luminosity fraction of the torus  $f_{\text{AGN}} = 69.8\% \pm 14.7\%$  ( $-0.156 \pm 0.113$  dex), as shown in the inset histogram.

leading goodness-of-fit achieved by CLUMPY. Therefore, previous torus parameters derived from CLUMPY (e.g., Nikutta et al. 2009; Audibert et al. 2017) should be treated with caution. The tendency for CLUMPY+BB to yield large inclinations can be understood. The BB component usually occupies as much near-IR emission as it can. The CLUMPY component is then biased toward longer wavelengths to compensate, which results in cooler temperatures and hence larger inferred inclinations (to block the inner hot dust emission).

In light of these factors, we henceforth only focus on parameters derived from the CAT3D-H-wind model, which is not only the most comprehensive and most physical, but, as discussed in Section 3.1, also can better capture the full complexities of the observed SEDs. Figure 5 examines the relation between the complementary angle of  $i$  and  $\theta$ . All the values are located on the lower-right region of the plot (i.e.  $\theta \geq 90^\circ - i$ ), as expected for type 1 AGNs that are observed almost face-on. This further reinforces our confidence in the physical robustness of the CAT3D-H-wind model. The properties of the torus for our sample are given in Table 1.

## 4. DISCUSSION

**Table 1.** Best-fit Parameters for the Torus Model

| Name          | $a$  | $h$ | $N_0$ | $i$          | $f_{\text{wd}}$ | $a_w$ | $\theta_w$   | $\theta_\sigma$ | $\log L$                | $\log L_{\text{total}}$ | $\log L_{\text{torus}}$ | $\log M_d$             |
|---------------|------|-----|-------|--------------|-----------------|-------|--------------|-----------------|-------------------------|-------------------------|-------------------------|------------------------|
|               |      |     |       | ( $^\circ$ ) |                 |       | ( $^\circ$ ) |                 |                         | ( $\text{erg s}^{-1}$ ) | ( $\text{erg s}^{-1}$ ) | ( $M_\odot$ )          |
| (1)           | (2)  | (3) | (4)   | (5)          | (6)             | (7)   | (8)          | (9)             | (10)                    | (11)                    | (12)                    | (13)                   |
| PG 0003 + 199 | −3.0 | 0.3 | 5.0   | 60           | 0.3             | −1.0  | 45           | 7.0             | $43.47^{+0.00}_{-0.01}$ | $44.49^{+0.00}_{-0.00}$ | $44.38^{+0.00}_{-0.00}$ | $6.32^{+0.03}_{-0.03}$ |
| PG 0007 + 106 | −3.0 | 0.2 | 10.0  | 30           | 0.75            | −1.0  | 45           | 7.0             | $43.84^{+0.01}_{-0.00}$ | $45.23^{+0.01}_{-0.01}$ | $45.01^{+0.01}_{-0.01}$ | $7.55^{+0.04}_{-0.05}$ |
| PG 0026 + 129 | −3.0 | 0.5 | 5.0   | 15           | 0.45            | −1.0  | 45           | 10.0            | $44.04^{+0.01}_{-0.01}$ | $45.31^{+0.01}_{-0.01}$ | $45.14^{+0.01}_{-0.01}$ | $6.97^{+0.21}_{-0.22}$ |
| PG 0049 + 171 | −3.0 | 0.5 | 5.0   | 0            | 0.75            | −1.5  | 45           | 7.0             | $42.96^{+0.01}_{-0.01}$ | $44.22^{+0.00}_{-0.01}$ | $44.07^{+0.01}_{-0.00}$ | $6.30^{+0.25}_{-0.18}$ |
| PG 0050 + 124 | −2.0 | 0.4 | 10.0  | 0            | 0.75            | −0.5  | 45           | 10.0            | $43.94^{+0.01}_{-0.00}$ | $45.64^{+0.00}_{-0.00}$ | $45.41^{+0.01}_{-0.00}$ | $8.21^{+0.01}_{-0.01}$ |
| PG 0052 + 251 | −3.0 | 0.3 | 7.5   | 60           | 0.45            | −1.0  | 45           | 7.0             | $44.31^{+0.01}_{-0.01}$ | $45.48^{+0.00}_{-0.01}$ | $45.33^{+0.01}_{-0.01}$ | $8.32^{+0.04}_{-0.02}$ |
| PG 0157 + 001 | −1.5 | 0.5 | 10.0  | 30           | 0.75            | −1.0  | 45           | 15.0            | $44.62^{+0.02}_{-0.02}$ | $46.27^{+0.01}_{-0.01}$ | $45.87^{+0.02}_{-0.02}$ | $8.63^{+0.04}_{-0.03}$ |
| PG 0804 + 761 | −3.0 | 0.3 | 7.5   | 15           | 1.0             | −0.5  | 30           | 7.5             | $44.44^{+0.02}_{-0.01}$ | $45.58^{+0.01}_{-0.01}$ | $45.52^{+0.01}_{-0.01}$ | $7.04^{+0.17}_{-0.17}$ |
| PG 0838 + 770 | −3.0 | 0.2 | 10.0  | 15           | 0.75            | −1.5  | 45           | 15.0            | $43.87^{+0.01}_{-0.01}$ | $45.26^{+0.00}_{-0.00}$ | $45.01^{+0.01}_{-0.01}$ | $8.18^{+0.03}_{-0.03}$ |
| PG 0844 + 349 | −2.5 | 0.2 | 10.0  | 15           | 0.75            | −1.0  | 45           | 10.0            | $43.31^{+0.01}_{-0.00}$ | $44.78^{+0.01}_{-0.00}$ | $44.63^{+0.00}_{-0.00}$ | $8.00^{+0.04}_{-0.05}$ |

NOTE—(1) Object name. (2) Power-law index. (3) Dimensionless scale height of Gaussian distribution for vertical distribution of clouds. (4) Average number of clouds along an equatorial line-of-sight. (5) Inclination. (6) Wind-to-disk ratio. (7) Radial distribution of dust clouds in the wind. (8) Half-opening angle of the wind. (9) Angular width of wind. (10) Luminosity normalization factor. (11) IR luminosity from 1 to 1000  $\mu\text{m}$ . (12) Torus luminosity from 1 to 1000  $\mu\text{m}$ . (13) Cold dust mass derived from DL07 model. Upper and lower values represent 84th and 16th percentile of the marginalized poster probability density function. Table 1 is published in its entirety in the machine-readable format. A portion is shown here for guidance regarding its form and content.

#### 4.1. Torus Luminosity and its Contribution to the Total IR Luminosity

Having established that we can robustly decompose the torus component from the overall IR SED, we are now able to study the torus luminosity ( $L_{\text{torus}}$ ), in particular its contribution to the total IR luminosity ( $L_{\text{IR}}$ ), which we define as the sum of all components from 1 to 1000  $\mu\text{m}$ . Appendix C shows that  $L_{\text{torus}}$  can be measured robustly in the SED decomposition. The correlation between the torus luminosity  $L_{\text{torus}}$  and the total IR luminosity  $L_{\text{IR}}$  is surprisingly tight (Figure 6), which indicates that for most of the objects the torus contributes a similar fraction of the total energy budget. The energy fraction is large. Defining  $f_{\text{AGN}} \equiv L_{\text{torus}}/L_{\text{IR}}$ ,  $\langle f_{\text{AGN}} \rangle = 69.8\% \pm 14.7\%$ . This result implies that the common practice of utilizing the integrated IR luminosity to estimate the star formation rates of AGN host galaxies may be highly biased, especially for powerful, high-redshift quasars.

#### 4.2. Correlation between Torus Luminosity and other AGN Bolometric Luminosity Tracers

In view of the significant fraction of the IR luminosity radiated by the torus, it is of interest to quantify the re-

lationship between the torus luminosity and other popularly employed tracers of AGN bolometric luminosity (Figure 7). A relatively tight (scatter  $\lesssim 0.3$  dex), essentially linear correlation holds between  $L_{\text{torus}}$  and the monochromatic continuum luminosity at 3000  $\text{\AA}$  ( $L_{3000}$ ; Baskin & Laor 2004), the monochromatic continuum luminosity at 5100  $\text{\AA}$  ( $L_{5100}$ ; Vestergaard & Peterson 2006), and the luminosity of the broad H $\beta$  emission line ( $L_{\text{H}\beta}$ ; Boroson & Green 1992). The strong correlation between  $L_{\text{torus}}$  and  $L_{3000}$  and  $L_{5100}$  simply reflects the fact that the torus is heated by the ultraviolet/optical continuum from the accretion disk. The correlation between  $L_{\text{torus}}$  and  $L_{\text{H}\beta}$ , on the other hand, is likely an indirect consequence of the more primary relation between the ultraviolet/optical continuum and the broad emission lines due to photoionization (e.g., Yee 1980; Greene & Ho 2005). The torus luminosity scales less well (scatter  $\sim 0.5$  dex) with the luminosity of [O III]  $\lambda 5007$   $\text{\AA}$  (Boroson & Green 1992) from the narrow-line region, presumably because of the complex dependence of [O III] strength on the intrinsic properties of the AGN (e.g., Eddington ratio; Shen & Ho 2014).

For convenience, we provide the relations between  $L_{\text{torus}}$  and  $L_{3000}$ ,  $L_{5100}$ ,  $L_{\text{H}\beta}$ , and  $L_{[\text{O III}]}$  obtained from

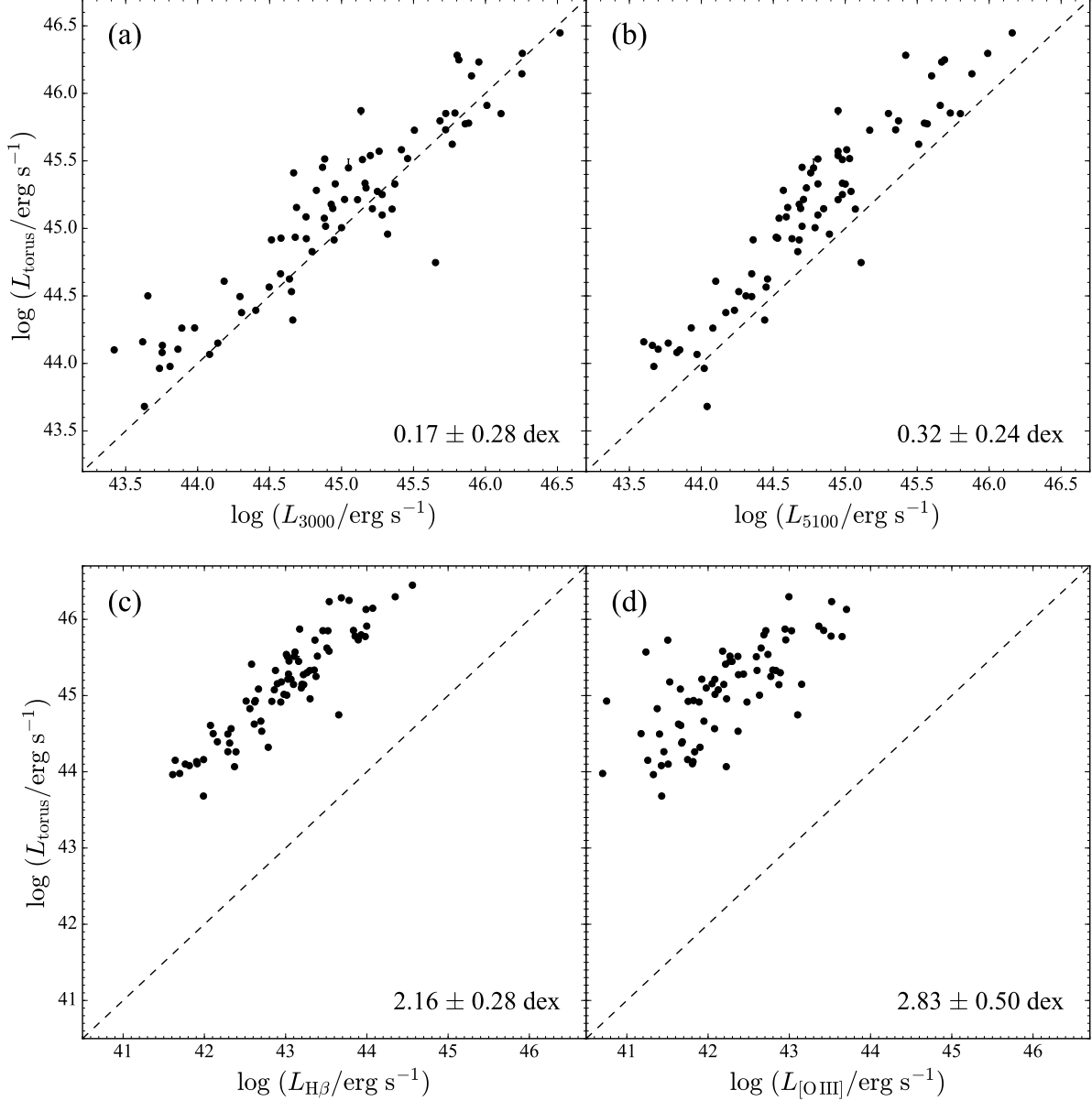


**Figure 7.** Correlation between  $L_{\text{torus}}$ , the luminosity of the torus derived from the CAT3D-H-wind model and (a)  $L_{3000}$ , the monochromatic luminosity at 3000 Å, (b)  $L_{5100}$ , the monochromatic luminosity at 5100 Å, (c)  $L_{H\beta}$ , the luminosity of broad  $H\beta$ , and (d)  $L_{[\text{O III}]}$ , the luminosity of  $[\text{O III}] \lambda 5007$ . Median and standard deviation are shown on the bottom-right corner of each panel, and the dashed line indicates a one-to-one correlation.

linear least-squares regression<sup>2</sup> method (Cappellari et al. 2013), in the form

$$\log \left( \frac{L_{\text{torus}}}{\text{erg s}^{-1}} \right) = a + b \times \left[ \log \left( \frac{L_X}{\text{erg s}^{-1}} \right) - X_0 \right] + \epsilon_{\text{int}}, \quad (1)$$

<sup>2</sup> The observational uncertainties for  $L_{3000}$ ,  $L_{5100}$ ,  $L_{H\beta}$ , and  $L_{[\text{O III}]}$  are assumed to be 20% on a linear scale (Baskin & Laor 2004; Vestergaard & Peterson 2006; Boroson & Green 1992). The uncertainties for  $L_{\text{torus}}$  is from the probability density function ( $\lesssim 10\%$  on a linear scale).

where  $\epsilon_{\text{int}}$  is the intrinsic scatter. The best-fit parameters for Equation 1 are given in Table 2.

#### 4.3. Properties of Objects with Strong Silicate Emission

Type 1 quasars commonly exhibit prominent silicate emission features at  $\sim 9.7\mu\text{m}$  and  $18\mu\text{m}$  (e.g., PG 1259+593; Figure 3). Among our sample of PG quasars, 53 have AGN-dominated mid-IR spectra ( $f_{\text{AGN}} > 50\%$ ) and strong silicate emission [ $\nu f_{\nu}(9.7\mu\text{m})/\nu f_{\nu}(14\mu\text{m}) > 1$ ]. We examine the torus prop-



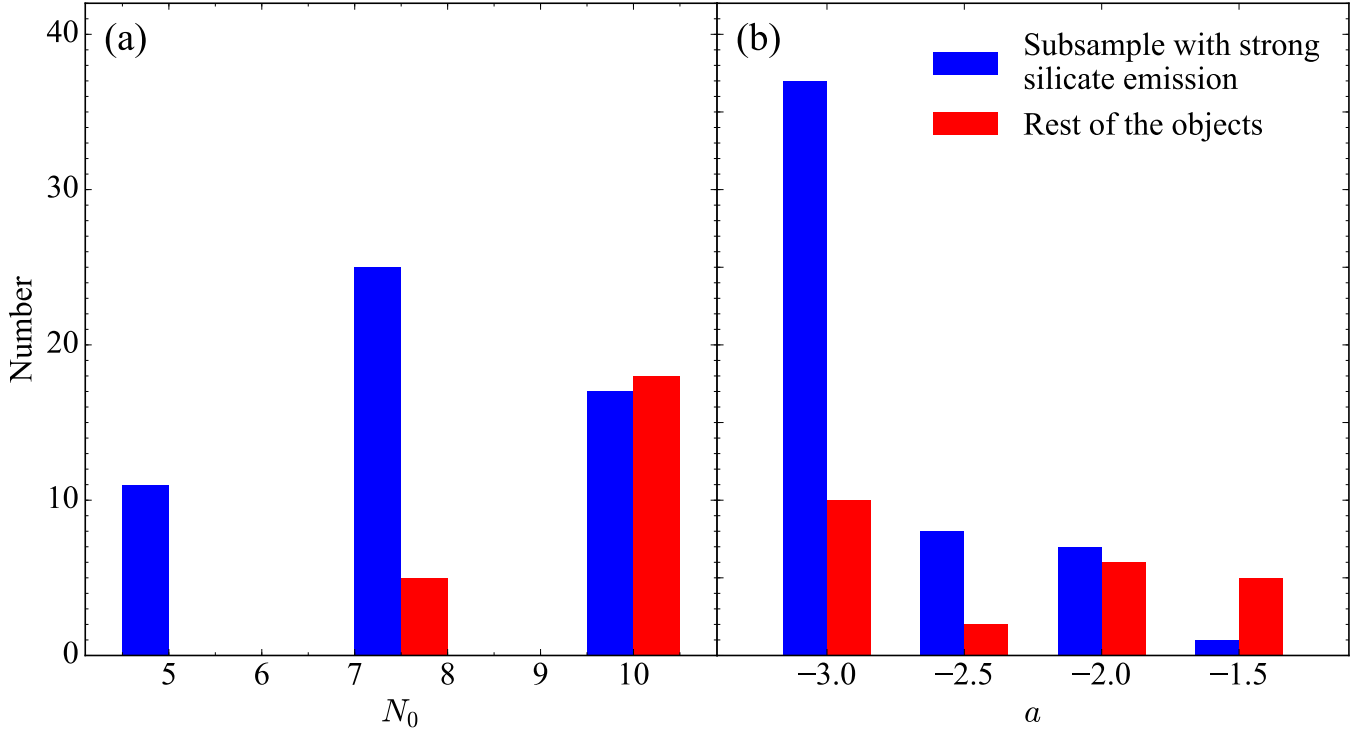


**Figure 8.** Comparison of the distributions of (a) number of clouds along the equatorial line-of-sight ( $N_0$ ) and (b) power-law index of radial density profile ( $a$ ) for the AGN-dominated subsample (blue) with strong silicate emission [ $\nu f_\nu(9.7\mu\text{m})/\nu f_\nu(14\mu\text{m}) > 1$  and  $f_{\text{AGN}} > 50\%$ ] and the rest of the objects (red).

**Table 2.** Best-fit Linear Regression Parameters for Equation 1

|                      | $a$                | $b$               | $X_0$ | $\epsilon_{\text{int}}$ |
|----------------------|--------------------|-------------------|-------|-------------------------|
| $L_{3000}$           | $45.120 \pm 0.026$ | $0.859 \pm 0.036$ | 44.95 | $0.225 \pm 0.022$       |
| $L_{5100}$           | $45.109 \pm 0.024$ | $1.022 \pm 0.039$ | 44.74 | $0.202 \pm 0.019$       |
| $L_{\text{H}\beta}$  | $45.171 \pm 0.023$ | $0.866 \pm 0.034$ | 43.03 | $0.191 \pm 0.019$       |
| $L_{[\text{O III}]}$ | $45.009 \pm 0.043$ | $0.781 \pm 0.064$ | 42.19 | $0.349 \pm 0.035$       |

erties of this physically interesting subsample. Figure 8 shows that objects with strong silicate emission preferentially have fewer clouds along the equatorial line-of-sight ( $N_0$ ) and a somewhat steeper power-law index ( $a$ ) for the radial density profile. A Kolmogorov-Smirnov test rejects the null hypothesis that the two subsamples are drawn from the same population with a probability of 0.0013 and 0.050, respectively. Taken at face value, this implies that objects with strong silicate emission have tori with a more centrally concentrated distribution of clouds. They also have fewer clouds along the line-of-sight to reradiate to longer wavelengths. This is consistent with the fact that most silicate-strong objects have very strong hot dust emission (Appendix B).

Although the best-fit torus parameters of individual objects have considerable uncertainty, the overall distribution of parameters are relatively robust (Appendix C).

#### 4.4. Anisotropic Emission from the Torus

Whereas the far-IR emission from the quasar host galaxy is isotropic and optically thin, the small-scale torus is optically thick and not spherically symmetric, resulting in anisotropic emission in the near-IR and mid-IR (Krolik & Begelman 1988; Pier & Krolik 1992). Thus, the inclination angle  $i$  of the torus should significantly affect its emission, both in terms of its luminosity and detailed spectral shape. When the number of clouds in the wind is small compared to that in the torus (e.g.,  $f_{\text{wd}} = 0.15$ ; Figure 9a), similar to the traditional picture of the torus, the SED and the flux of the torus change systematically and strongly with  $i$ , in the sense that the average dust temperature and luminosity decrease with increasing  $i$ . The opposite regime when the number of clouds is much larger in the wind than in the torus (e.g.,  $f_{\text{wd}} = 2.25$ ; Figure 9b) presents a very different situation. The observed torus energy first decreases and the SED softens as  $i$  increases, and then it reverses direction, as a consequence of the wind emission becoming more prominent with increasing  $i$  (see also Section 3.1).

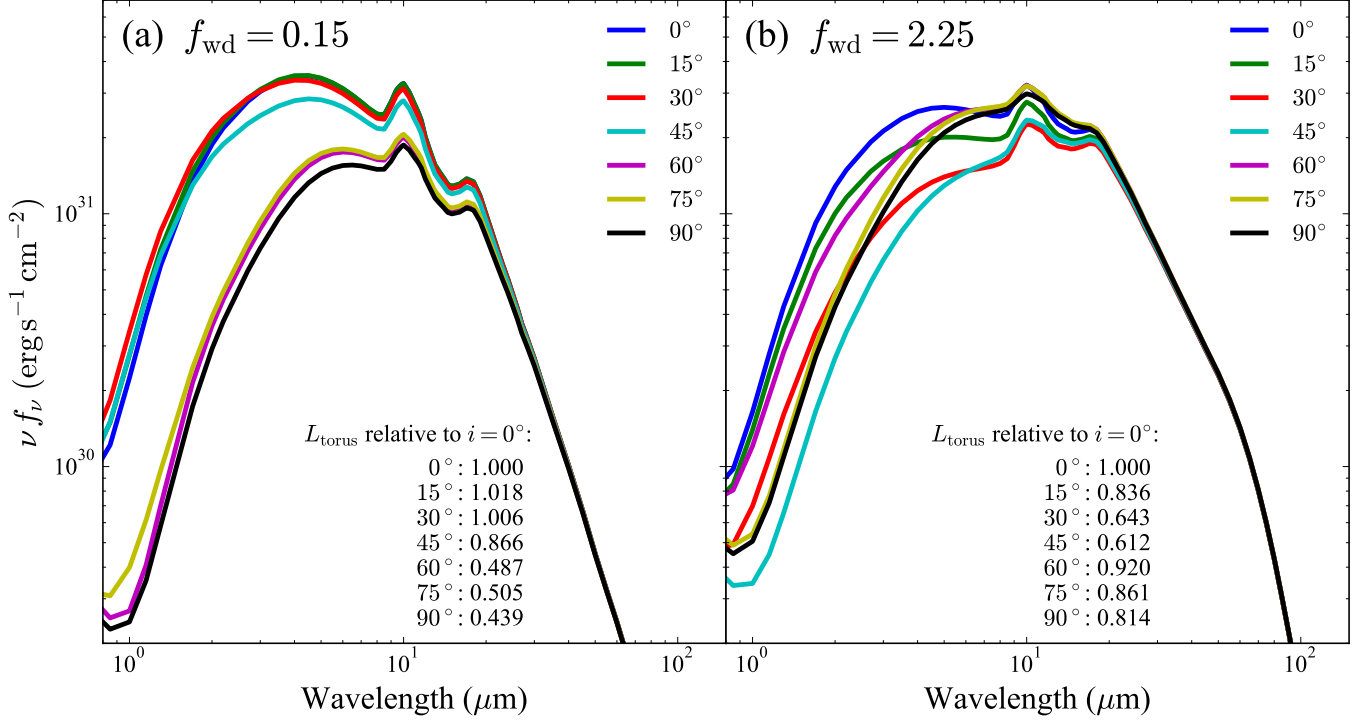


**Figure 9.** The influence of the inclination angle  $i$  ( $0^\circ$  to  $90^\circ$ ) on the torus SED, for the CAT3D-H-wind model computed with (a)  $f_{\text{wd}} = 0.15$  and (b)  $f_{\text{wd}} = 2.25$ , with all other model parameters fixed ( $N = 5$ ,  $a = -3.00$ ,  $h = 0.50$ ,  $a_w = -2.00$ ,  $\theta_w = 30^\circ$ , and  $\theta_\sigma = 15.00$ ). The fluxes are scaled to a sublimation radius of 0.29 pc. The legend on the bottom part shows the IR (1–1000  $\mu\text{m}$ ) luminosity of the torus for each specific  $i$ , relative to  $i = 0^\circ$ .

In cases of extremely large values of  $f_{\text{wd}}$ , the wind component dominates the mid-IR, compensating for or even exceeding the loss of hot emission from the torus.

Not all quasars are viewed face-on (Figure 4). As a corollary to the sensitivity of the torus emission to  $i$ , the intrinsic, total luminosity of the torus itself depends on  $i$ . For example, the observed luminosity of a quasar with  $f_{\text{wd}} = 2.25$  and  $i = 45^\circ$  is underestimated by nearly a factor of 2 compared to its intrinsic luminosity (at  $i = 0^\circ$ ; Figure 9b). This implies that the value of  $\langle f_{\text{AGN}} \rangle \approx 70\%$  (Figure 6) is most likely a lower limit.

#### 4.5. The Dependence of Torus Opening Angle on Eddington Ratio

The structure of the torus has long been suspected to change with the physical properties of the AGN. The most widely discussed concept is that of a receding torus (Lawrence 1991; Simpson 2005; Hönig & Beckert 2007), whereby the torus covering factor decreases with increasing  $L_{\text{bol}}$ , which manifests itself observationally as an enhanced fraction of type 1 AGNs at higher luminosity. This picture has also enjoyed support from studies that parameterize the torus covering factor using the relative luminosity output of the torus, finding that  $L_{\text{torus}}/L_{\text{bol}}$  decreases with increasing AGN luminosity (Maiolino et al. 2007; Treister et al. 2008; Lusso et al. 2013). More

recently, Ricci et al. (2017), analyzing a large sample of hard X-ray-selected AGNs, proposed that the torus covering factor depends primarily not on luminosity but instead on Eddington ratio,  $\lambda_{\text{Edd}} = L_{\text{bol}}/L_{\text{Edd}}$ , where  $L_{\text{Edd}} = 1.26 \times 10^{38} (M_{\text{BH}}/M_\odot)$ . Radiation pressure acting on dust grains expels obscuring material, causing the fraction of obscured AGNs—defined in terms of X-ray absorbing column density—to decrease with increasing  $\lambda_{\text{Edd}}$ .

Previous studies of the torus covering factor for PG quasars have yielded contradictory results. Analyzing a sample of 64 PG quasars, Cao (2005) found no obvious dependence between  $L_{\text{NIR}}/L_{\text{bol}}$  and  $\lambda_{\text{Edd}}$  or  $L_{\text{bol}}$ . By contrast, Mor et al. (2009), fitting the SEDs of a subset of 26 PG quasars using the CLUMPY torus model (with no additional BB component), reported a relatively strong correlation between the model-derived covering factor and  $L_{\text{bol}}$ . We re-examine these trends using our larger sample of PG quasars, analyzed with the most updated torus models, using the BH masses and bolometric luminosities compiled in Shanguan et al. (2018). Consistent with Cao (2005), we also see no convincing relation between  $L_{\text{torus}}/L_{\text{bol}}$  and  $L_{\text{bol}}$  or  $\lambda_{\text{Edd}}$  (Figure 10). As pointed out by Stalevski et al. (2016), the intrinsic anisotropy of the torus makes it difficult

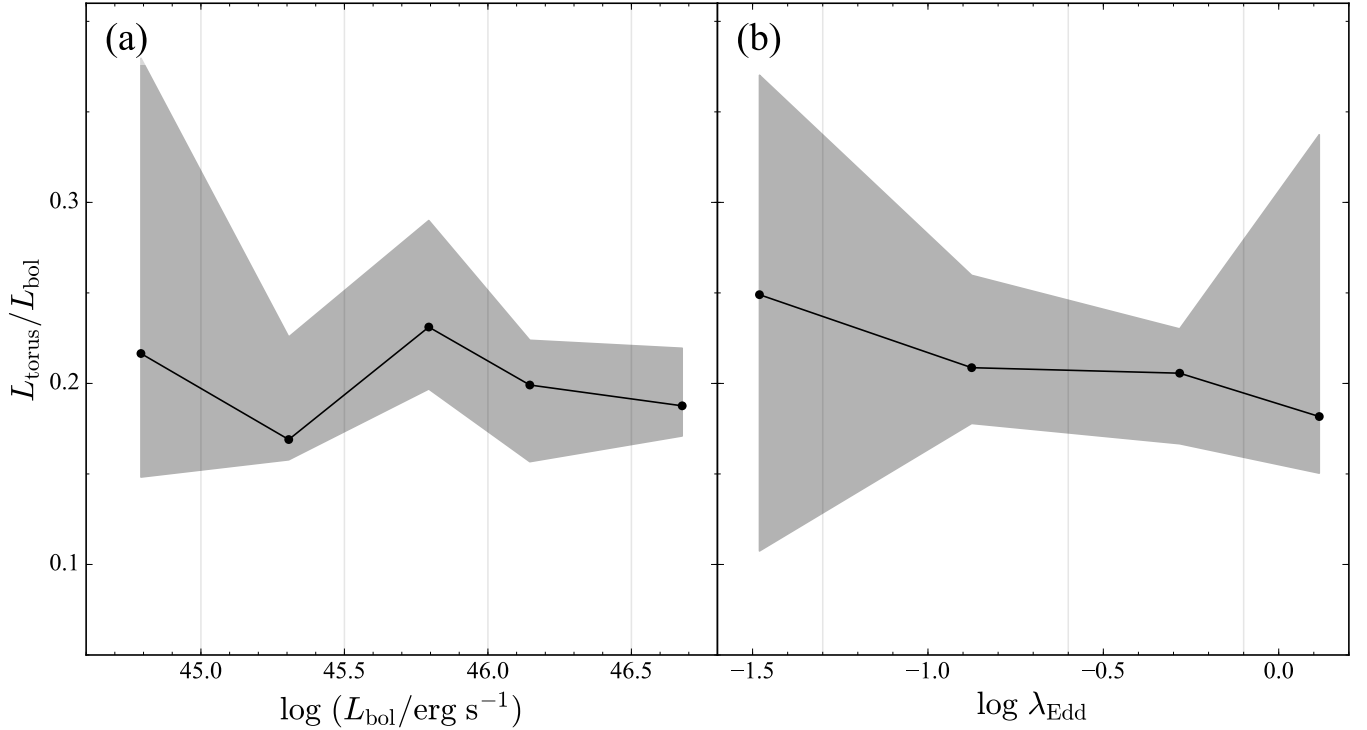


**Figure 10.** The dependence of torus luminosity fraction,  $L_{\text{torus}}/L_{\text{bol}}$ , on (a) bolometric luminosity  $L_{\text{bol}}$  and (b) Eddington ratio  $\lambda_{\text{Edd}}$ . The sample is divided into bins with the boundaries as indicated by the vertical lines. The points are the median values of the bins, with the shaded area representing the 25th and 75th percentage value of the bins.

to estimate the torus covering factor accurately from  $L_{\text{torus}}/L_{\text{bol}}$ .

We suggest that the best parameter to describe the torus covering factor is the torus half-opening angle  $\theta$ , as it directly relates to the actual geometry of the torus, independent of inclination. Figure 11 reveals an intriguing trend:  $\theta$  decreases as the Eddington ratio increases from  $\log \lambda_{\text{Edd}} \approx -2.0$  to  $\log \lambda_{\text{Edd}} \approx -0.25$ ; then,  $\theta$  rises again as  $\log \lambda_{\text{Edd}}$  increases from  $-0.25$  to  $\sim 0.5$ . The large scatter is due to the discreteness of the parameter space, the small number of objects in the sample, as well as to the significant uncertainties of the derived parameters from the torus model (Appendix C). Despite these limitations, we believe that the trends are robust.

The structure of the accretion disk around a BH changes in response to changes in the mass accretion rate. Three main regimes are commonly recognized: (1) an optically thin, geometrically thick, radiative inefficient flow at very low accretion rates ( $\lambda_{\text{Edd}} \lesssim 0.01$ ; Narayan & Yi 1994; Yuan & Narayan 2014, and references therein); (2) an optically thick, geometrically thin, standard disk at intermediate accretion rates ( $0.01 \lesssim \lambda_{\text{Edd}} \lesssim 0.1$ ; Shakura & Sunyaev 1973; Kato et al. 1998, and references therein); and (3) an optically thick, geometrically thick, slim disk at very high accretion rates ( $\lambda_{\text{Edd}} \gtrsim 0.3$ ; Begelman 1978; Abramowicz et al. 1988,

and references therein). The relationship between the torus opening angle and Eddington ratio may arise from the interplay between the illumination pattern of the central accretion disk and its surrounding torus. Consider the schematic sketched in Figure 12. When  $\lambda_{\text{Edd}}$  is low enough for the accretion flow to be radiatively inefficient (not illustrated), the deficit of ultraviolet photons in its SED (Ho 1999, 2008) implies that a large fraction of the dusty gas (if present; see She et al. 2018) cannot be evacuated by radiation pressure, resulting in a large torus covering factor. With increasing  $\lambda_{\text{Edd}}$  the accretion disk enters the standard regime, and its large ultraviolet output can efficiently clear away the obscuring material, leading to a systematic decrease in  $\theta$ . Finally, when  $\lambda_{\text{Edd}}$  crosses above the threshold for a slim disk, its vertically thick inner funnel results in significant anisotropy of its ionizing radiation field (Abramowicz et al. 1988; Wang et al. 2014), which again leads to an increase in  $\theta$ . Note that a natural corollary of this model is that highly accreting (super-Eddington) AGNs should contain a larger fraction of type 2 sources.

Our schematic picture is qualitatively consistent with but expands upon the scenario proposed by Ricci et al. (2017), primarily by extending the dynamic range to  $\lambda_{\text{Edd}} > 1$ , since the PG quasar sample contains a sizable fraction of highly accreting sources. By the same to-

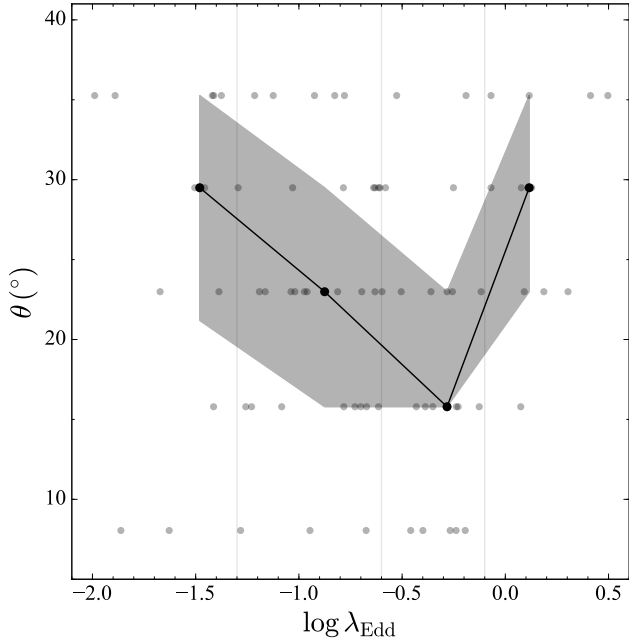


**Figure 11.** Dependence of the torus half-opening angle  $\theta$  on Eddington ratio  $\lambda_{\text{Edd}}$  derived from best-fitting results using the CAT3D-H-wind torus model. The grey dots in the background represent individual objects. To better visualize any possible trends, we bin the sample into four bins of  $\lambda_{\text{Edd}}$ , whose boundaries are indicated by the vertical lines. The black points are the median values of the four bins, with the shaded area representing the 25th and 75th percentage value of their bins.

ken, Ricci et al.’s sample, selected by hard X-rays from *Swift*/BAT observations, extends  $\lambda_{\text{Edd}}$  to significantly lower values than our sample. Hence our two studies are highly complementary.

## 5. CONCLUSIONS

We apply a newly developed Bayesian MCMC method to study the IR ( $1-500\ \mu\text{m}$ ) SEDs of a large, well-defined sample of low-redshift ( $z < 0.5$ ) Palomar-Green quasars. Our primary motivation is to quantify the properties of the AGN-heated dust, by decomposing the SEDs using a combination of physically motivated emission components for the stars, torus, and large-scale dust component of the host galaxy. Our extensive tests of a suite

of theoretical templates indicate that the majority of the quasar SEDs can be best fitted with the torus models of Hönig & Kishimoto (2017, CAT3D) that properly account for the different sublimation temperatures of silicate and graphite grains and consider a polar wind component.

Our main conclusions are the following:

1. The luminosity of the torus correlates tightly with the total IR ( $1-1000\ \mu\text{m}$ ) luminosity. On average,  $\langle L_{\text{torus}}/L_{\text{IR}} \rangle \approx 70\%$ . Star formation rates of quasar host galaxies estimated using  $L_{\text{IR}}$  will be significantly overestimated if the contribution from the torus is not properly taken into account.
2. The luminosity of the torus correlates tightly (scatter  $< 0.3$  dex) with the luminosity of the ultraviolet/optical continuum and the broad H $\beta$  emission line, indicating a close link between the central ionization source and re-radiation by the torus.
3. The majority of the torus inclination angles lie in the range  $\lesssim 45^\circ$ , consistent with expectations for type 1 (broad-line) AGNs.
4. Most PG quasars (53/76) show both strong hot dust emission and silicate features, which can be used to differentiate dust torus models.
5. The torus covering factor, as reflected in the torus half-opening angle  $\theta$ , decreases with increasing Eddington ratio until  $\lambda_{\text{Edd}} \approx 0.5$ , above which  $\theta$  rises again. We suggest that these trends can be explained by the pattern of the radiation field impinging upon the torus from the accretion disk, which transitions from a standard thin disk to a slim disk at the highest accretion rates.

We thank the referee, M. Kishimoto, for his stimulating comments and suggestions that helped to improve the quality and presentation of our paper. This work was supported by the National Key R&D Program of China (2016YFA0400702) and the National Science Foundation of China (11473002, 11721303, 11403072).

## REFERENCES

- Abramowicz, M. A., Czerny, B., Lasota, J. P., & Szuszkiewicz, E. 1988, *ApJ*, 332, 646
- Alonso-Herrero, A., Ramos Almeida, C., Mason, R., et al. 2011, *ApJ*, 736, 82
- Antonucci, R. 1993, *ARA&A*, 31, 473
- Audibert, A., Riffel, R., Sales, D. A., Pastoriza, M. G., & Ruschel-Dutra, D. 2017, *MNRAS*, 464, 2139
- Barvainis, R. 1987, *ApJ*, 320, 537
- Baskin, A., & Laor, A. 2004, *MNRAS*, 350, L31
- Begelman, M. C. 1978, *MNRAS*, 184, 53

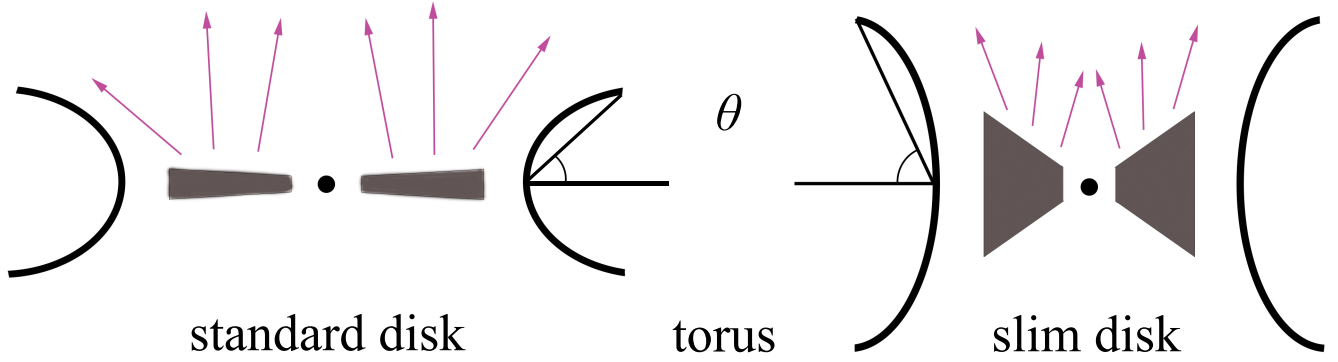


**Figure 12.** Schematic illustration to explain the variation of torus covering factor (half-opening angle  $\theta$ ) with Eddington ratio (Figure 11). For moderate accretion rates, the emission from the standard optically thick, geometrically thin accretion disk (left) can suppress the vertical height (and hence covering factor) of the torus. At very high or super-Eddington accretion rates, the radiation from the optically and geometrically thick slim disk (right) is anisotropic and more collimated perpendicular to the torus, resulting in large covering factor for the torus.

- Borison, T. A., & Green, R. F. 1992, *ApJS*, 80, 109
- Brightman, M., & Ueda, Y. 2012, *MNRAS*, 423, 702
- Bruzual, G., & Charlot, S. 2003, *MNRAS*, 344, 1000
- Cao, X. 2005, *ApJ*, 619, 86
- Cappellari, M., Scott, N., Alatalo, K., et al. 2013, *MNRAS*, 432, 1709
- Chabrier, G. 2003, *PASP*, 115, 763
- Deo, R. P., Richards, G. T., Nikutta, R., et al. 2011, *ApJ*, 729, 108
- Draine, B. T., & Li, A. 2007, *ApJ*, 657, 810
- Dullemond, C. P., & van Bemmelen, I. M. 2005, *A&A*, 436, 47
- Efstathiou, A., & Rowan-Robinson, M. 1995, *MNRAS*, 273, 649
- Ezhikode, S. H., Gandhi, P., Done, C., et al. 2017, *MNRAS*, 472, 3492
- García-González, J., Alonso-Herrero, A., Hönig, S. F., et al. 2017, *MNRAS*, 470, 2578
- Greene, J. E., & Ho, L. C. 2005, *ApJ*, 630, 122
- Ho, L. C. 1999, *ApJ*, 516, 672
- . 2008, *ARA&A*, 46, 475
- Hönig, S. F., & Beckert, T. 2007, *MNRAS*, 380, 1172
- Hönig, S. F., Beckert, T., Ohnaka, K., & Weigelt, G. 2006, *A&A*, 452, 459
- Hönig, S. F., & Kishimoto, M. 2017, *ApJL*, 838, L20
- Hönig, S. F., Kishimoto, M., Gandhi, P., et al. 2010, *A&A*, 515, A23
- Hönig, S. F., Kishimoto, M., Tristram, K. R. W., et al. 2013, *ApJ*, 771, 87
- Kato, S., Fukue, J., & Mineshige, S., eds. 1998, *Black-hole accretion disks*
- Kishimoto, M., Hönig, S. F., Beckert, T., & Weigelt, G. 2007, *A&A*, 476, 713
- Krolik, J. H., & Begelman, M. C. 1988, *ApJ*, 329, 702
- Lawrence, A. 1991, *MNRAS*, 252, 586
- López-Gonzaga, N., & Jaffe, W. 2016, *A&A*, 591, A128
- López-Gonzaga, N., Jaffe, W., Burtscher, L., Tristram, K. R. W., & Meisenheimer, K. 2014, *A&A*, 565, A71
- Lusso, E., Hennawi, J. F., Comastri, A., et al. 2013, *ApJ*, 777, 86
- Lynden-Bell, D. 1969, *Nature*, 223, 690
- Maiolino, R., Shemmer, O., Imanishi, M., et al. 2007, *A&A*, 468, 979
- Mor, R., & Netzer, H. 2012, *MNRAS*, 420, 526
- Mor, R., Netzer, H., & Elitzur, M. 2009, *ApJ*, 705, 298
- Narayan, R., & Yi, I. 1994, *ApJL*, 428, L13
- Nenkova, M., Sirocky, M. M., Ivezić, Ž., & Elitzur, M. 2008a, *ApJ*, 685, 147
- Nenkova, M., Sirocky, M. M., Nikutta, R., Ivezić, Ž., & Elitzur, M. 2008b, *ApJ*, 685, 160
- Netzer, H. 2015, *ARA&A*, 53, 365
- Nikutta, R., Elitzur, M., & Lacy, M. 2009, *ApJ*, 707, 1550
- Pe’er, A. 2014, *SSRv*, 183, 371
- Pier, E. A., & Krolik, J. H. 1992, *ApJ*, 401, 99
- Planck Collaboration, Ade, P. A. R., Aghanim, N., et al. 2016, *A&A*, 594, A13
- Raban, D., Jaffe, W., Röttgering, H., Meisenheimer, K., & Tristram, K. R. W. 2009, *MNRAS*, 394, 1325
- Rees, M. J. 1984, *ARA&A*, 22, 471
- Ricci, C., Trakhtenbrot, B., Koss, M. J., et al. 2017, *Nature*, 549, 488
- Schartmann, M., Meisenheimer, K., Camenzind, M., et al. 2008, *A&A*, 482, 67
- Schmidt, M., & Green, R. F. 1983, *ApJ*, 269, 352
- Shakura, N. I., & Sunyaev, R. A. 1973, *A&A*, 24, 337
- Shangguan, J., Ho, L. C., & Xie, Y. 2018, *ApJ*, 854, 158
- She, R., Ho, L. C., Feng, H., & Cui, C. 2018, *ApJ*, in press (arXiv:1804.07482)
- Shen, Y., & Ho, L. C. 2014, *Nature*, 513, 210



- Siebenmorgen, R., Heymann, F., & Efstathiou, A. 2015, A&A, 583, A120
- Simpson, C. 2005, MNRAS, 360, 565
- Stalevski, M., Fritz, J., Baes, M., Nakos, T., & Popović, L. Č. 2012, MNRAS, 420, 2756
- Stalevski, M., Ricci, C., Ueda, Y., et al. 2016, MNRAS, 458, 2288
- Treister, E., Krolik, J. H., & Dullemond, C. 2008, ApJ, 679, 140
- Tristram, K. R. W., Meisenheimer, K., Jaffe, W., et al. 2007, A&A, 474, 837
- Ueda, Y., Eguchi, S., Terashima, Y., et al. 2007, ApJL, 664, L79
- Urry, C. M., & Padovani, P. 1995, PASP, 107, 803
- Vestergaard, M., & Peterson, B. M. 2006, ApJ, 641, 689
- Wang, J.-M., Qiu, J., Du, P., & Ho, L. C. 2014, ApJ, 797, 65
- Xie, Y., Li, A., & Hao, L. 2017, ApJS, 228, 6
- Yee, H. K. C. 1980, ApJ, 241, 894
- Yuan, F., & Narayan, R. 2014, ARA&A, 52, 529

## APPENDIX

## A. INFLUENCE OF DIFFERENT TORUS MODELS ON THE DERIVED DUST MASSES

Our fitting code derives, as a by-product, the interstellar cold dust mass  $M_d$  from the DL07 model. Figure 13 shows the effect on  $M_d$  of choosing different torus models for the SED fitting, using, as reference, the CLUMPY model. As long as the far-IR peak of the SED is well constrained, no significant difference is found on  $M_d$ . Any systematic deviations are at the level of  $\lesssim 0.05$  dex, with standard deviations of  $\sim 0.1 - 0.3$  dex. This is consistent with the results of Shangguan et al. (2018), who compared the effect on  $M_d$  from the use of the CLUMPY torus model and another torus model by Xie et al. (2017).

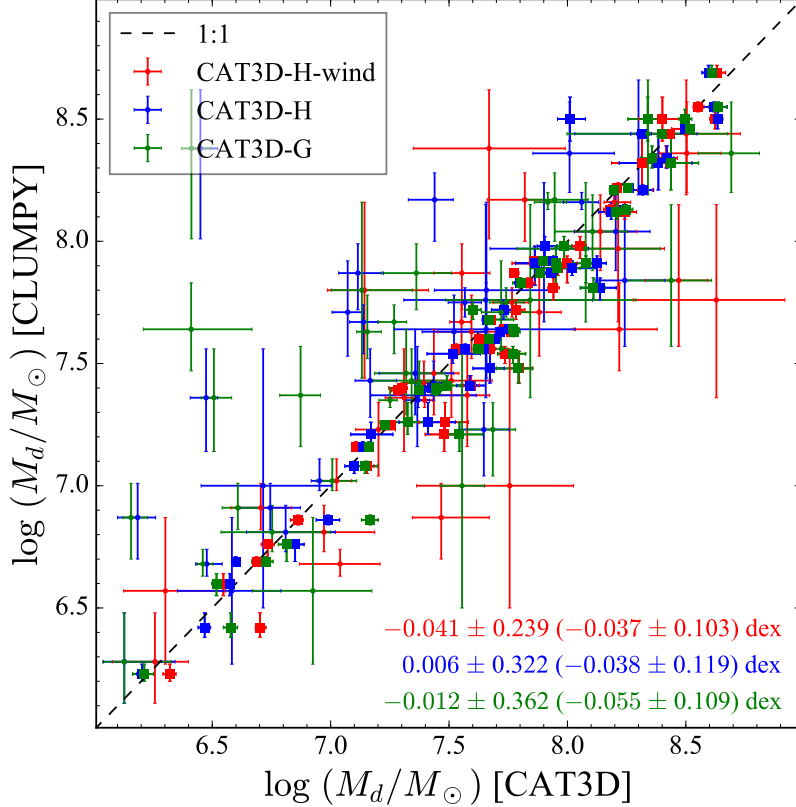


**Figure 13.** Comparison of cold dust masses for the host galaxy derived with different torus models. Colors are the same as Figure 4. Large points represent objects with SEDs whose far-IR peak is well-constrained by the *Herschel* data; smaller points do not have well-constrained far-IR peaks. The residuals and standard deviations are given in the lower-right corner; values in parentheses are for the objects with SEDs with well-constrained far-IR peaks.

## B. GOODNESS-OF-FIT OF DIFFERENT TORUS MODELS

We use the reduced  $\chi^2_\nu$  ( $\chi^2$  per degree of freedom) to assess quantitatively the relative goodness-of-fit of the different torus models. As the *Spitzer*/IRS spectrum covers the spectral range that maximally constrains the dust torus, we restrict the  $\chi^2_\nu$  calculation to the wavelength region  $\sim 5 - 38 \mu\text{m}$  (in the observed frame). For cases without strong silicate features and hot dust emission (e.g., PG 0934+013; Figure 2), all the models provide similarly acceptable fits. A large fraction of the objects, however, resemble PG 1259+593 (Figure 3), for which the CAT3D-H-wind model clearly exhibits a much lower  $\chi^2_\nu$  than the other models<sup>3</sup>. To compare the different models quantitatively, we group the  $\chi^2_\nu$  values into five bins: 0–50, 50–100, 100–500, 500–1000, and >1000. Figure 14 shows that more than half of

<sup>3</sup> The notable exception is the CLUMPY+BB model, which, despite its flexibility, is disfavored because of the ad hoc nature of the BB component (Section 3.1).

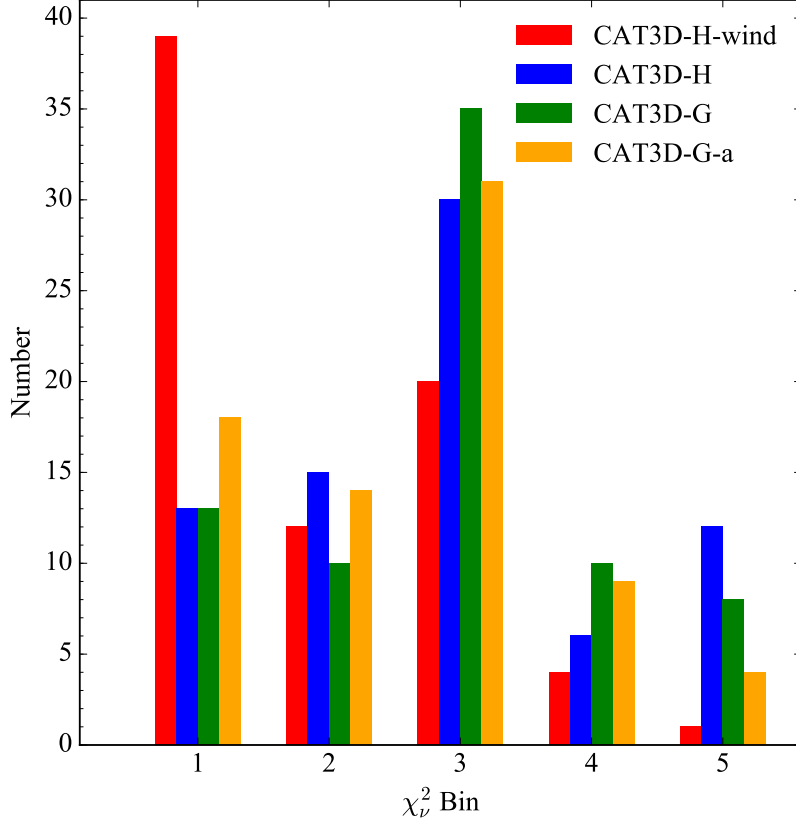


**Figure 14.** Histogram of  $\chi^2_\nu$  of fitting results for the CAT3D-H-wind (red), CAT3D-H (blue), CAT3D-G (green), and CAT3D-G-a (orange) torus models. Bins for  $\chi^2_\nu$  are (1) 0–50, (2) 50–100, (3) 100–500, (4) 500–1000, and (5) >1000.

the objects fit using CAT3D-H-wind have  $\chi^2_\nu < 50$ . Figure 2 illustrates that  $\chi^2_\nu \approx 50$  already signifies a very good fit. By contrast, the other three CAT3D models that lack a wind component have  $\chi^2_\nu$  distributions that peak in the range  $\sim 100 - 500$ , nearly an order of magnitude larger than the wind model. In extreme cases such as PG 1259+593 (Figure 3), the wind model provides exceptionally good fits with  $\chi^2_\nu \approx 10$ , unquestionably superior to the non-wind models. Thus, we conclude, based on the sample as a whole and on certain individual cases, that the CAT3D torus models that incorporate a wind component best match the mid-IR SEDs of our sample of quasars.

What aspects of the mid-IR SED actually distinguish the wind model from the others? Two prominent features stand out in our quasar sample: hot dust continuum emission at  $\sim 5 \mu\text{m}$  and strong silicate emission at  $\sim 9.7$  and  $18 \mu\text{m}$ . We use the flux ratio of the continuum emission at  $6 \mu\text{m}$ <sup>4</sup> and  $14 \mu\text{m}$  to indicate the relative strength of the hot dust emission, and the flux ratio of the  $9.7 \mu\text{m}$  silicate emission to that of the  $14 \mu\text{m}$  continuum emission to gauge the relative strength of the silicate features. Figure 15 shows these flux ratios for the 38 PG quasars with  $f_{\text{AGN}} > 69.8\%$  (median value of the whole sample) derived from the observed spectrum. Our quasar sample exhibits hot dust emission and silicate emission of comparable relative strength: the median value of  $\nu f_\nu(6\mu\text{m})/\nu f_\nu(14\mu\text{m}) \approx 1.18$  and  $\nu f_\nu(9.7\mu\text{m})/\nu f_\nu(14\mu\text{m}) \approx 1.16$ . The two ratios show a relatively strong correlation with a Pearson’s correlation coefficient of  $r \approx 0.8$  and a  $p$ -value of  $\sim 10^{-9}$ . For comparison, we overlay the flux ratios computed from the theoretical template spectra for the four versions of the CAT3D models. The non-wind models (Figure 15, panels (a)–(c)) cover little of the observed parameter space of the PG quasars, whereas the CAT3D-H-wind templates cover most of it (panel (d)). Objects whose flux ratios are not covered by the CAT3D-H-wind templates have relatively worse fits. Two non-wind models (CAT3D-G and CAT3D-H), would always predict much stronger silicate emission for a given hot dust strength. For torus models that only have a toroidal structure, the spatial distributions of the graphite and silicate dust are coupled, except for temperatures  $> 1200$  K. The observed strong hot dust emission requires the

<sup>4</sup> In order to be covered by *Spitzer*/IRS spectrum and avoid possible PAH emission.

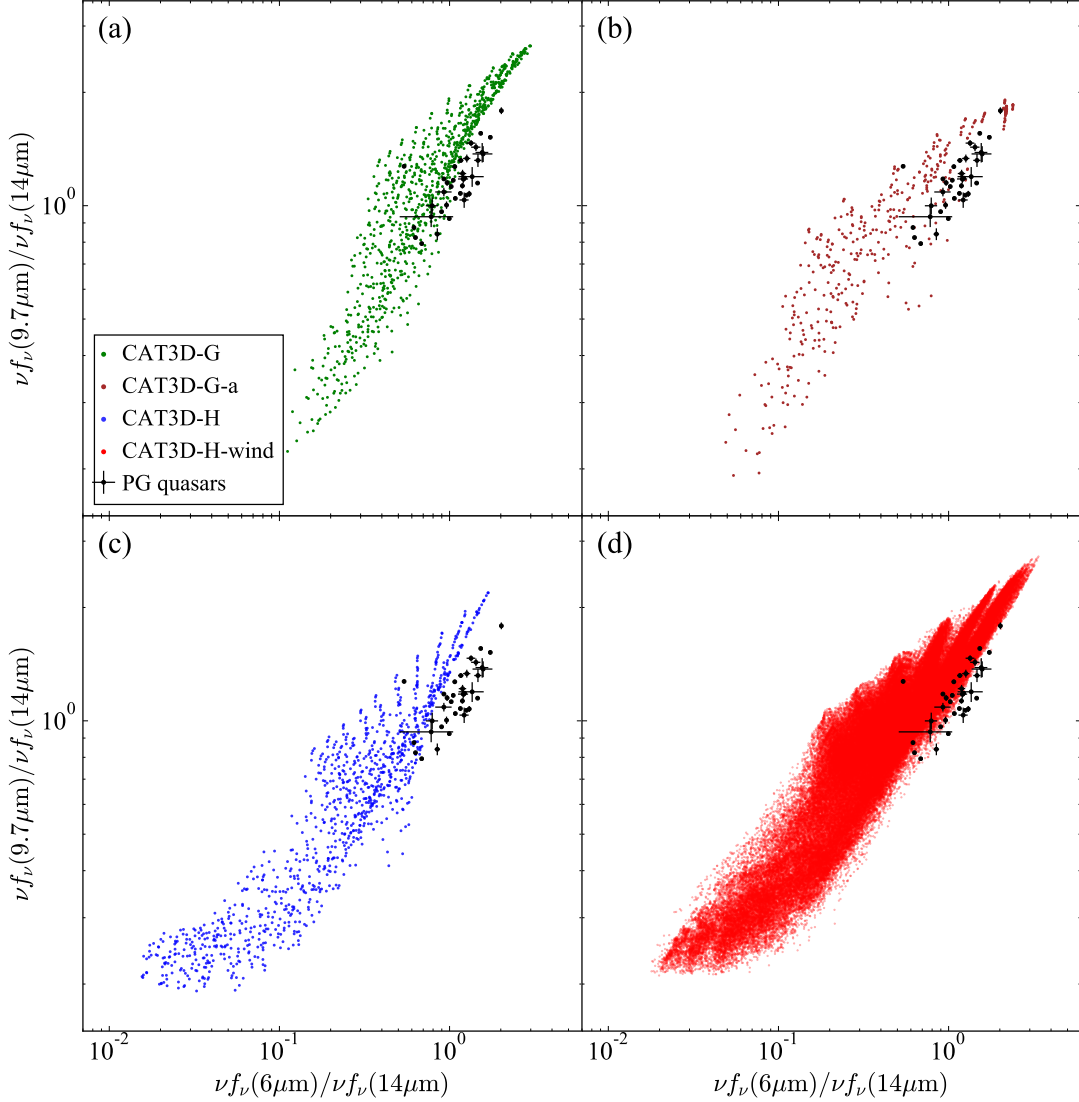


**Figure 15.** Comparison of different model coverages of strength of hot dust  $[\nu f_\nu(6\mu\text{m})/\nu f_\nu(14\mu\text{m})]$  and silicates  $[\nu f_\nu(9.7\mu\text{m})/\nu f_\nu(14\mu\text{m})]$  for our sample. Model coverage of CAT3D-G, CAT3D-G-a, CAT3D-H, and CAT3D-H-wind are shown in panels (a) to (d), respectively. “PG quasars” represents the values derived from *Spitzer*/IRS spectrum for objects with AGN fraction ( $f_{\text{AGN}}$ ) above the median value of the whole sample.

model to have a highly concentrated dust distribution. As the clump distribution is described by a power law, the silicates will have the same centrally concentrated distribution as the graphite and will be heated to high temperature. The introduction of an extra wind component, however, contributes more hot graphite emission without boosting the strength of the silicate emission (Hönig & Kishimoto 2017). The poor coverage of CAT3D-G-a model is possibly due to the limited number of templates.

### C. SENSITIVITY OF PARAMETERS TO THE DATA

We use mock data to test the robustness of our fitting results and explore the sensitivity of the parameters to the data, taking comprehensive uncertainties into account. Following the methodology of Shangguan et al. (2018), we generate two groups of mock SEDs using the best-fit CAT3D-H-wind models of the real PG quasar SEDs. The two groups of mock SEDs are generated as follows<sup>5</sup>:

<sup>5</sup> We exclude three objects lacking complete measurements in all six *Herschel* bands.

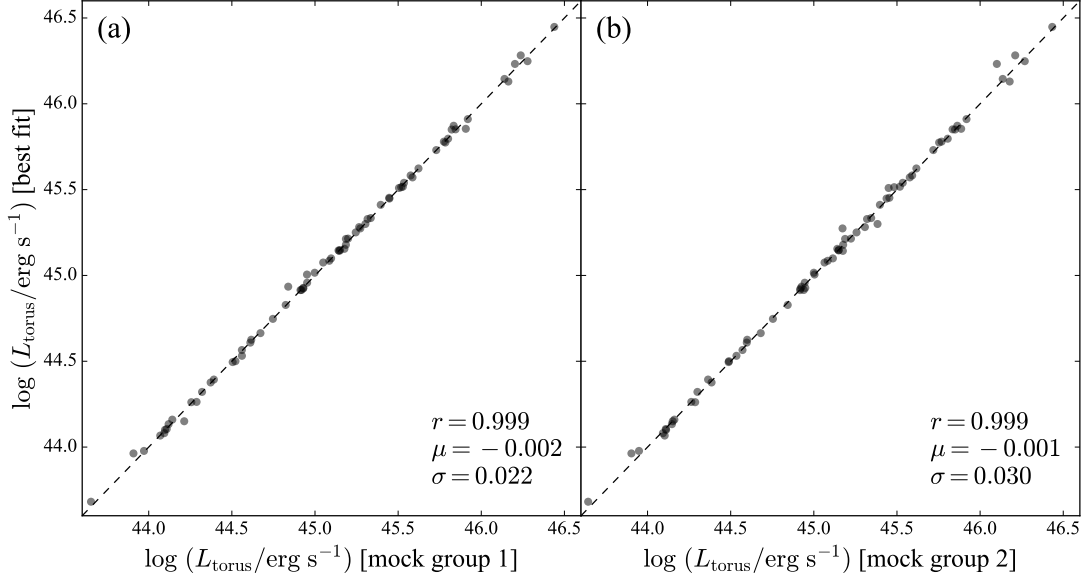


**Figure 16.** Comparison of torus luminosity  $L_{\text{torus}}$  from the best fit with that from (a) mock group 1 and (b) mock group 2. The legend gives the Pearson's correlation coefficient ( $r$ ), median ( $\mu$ ), and standard deviation ( $\sigma$ ).

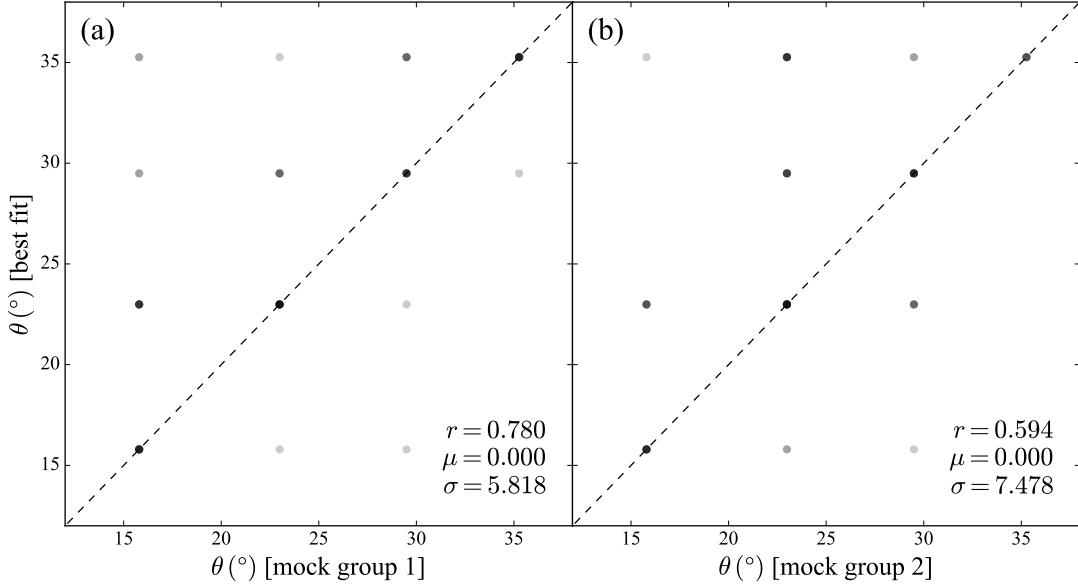


**Figure 17.** Same as Figure 16, but for half-opening angle  $\theta$ .

1. We use the best-fit parameters of each quasar to generate the SED model. The mock data are calculated from the SED model, perturbed according to their uncertainties from the observed data, assuming a Gaussian distribution with standard deviation equal to their uncertainties.
2. We use the values from (1) but add systematic uncertainty to the photometry and spectrum to account for calibration uncertainties, assuming a Gaussian distribution with different standard deviations: 5% for *Spitzer*/IRS, 3% for 2MASS and *WISE*, and 5% for *Herschel*/PACS and SPIRE. The systematic uncertainty for each band from the same data set is the same (e.g., the uncertainties for the  $J$ ,  $H$ , and  $K_s$  bands of 2MASS are the same). Then, we substitute the values for the *Herschel* bands with upper limits if these bands are not detected in the real data.



We fit the two groups of mock SEDs using the CAT3D-H-wind model. The fit results are globally very good. For group 1, the best-fit models are always indistinguishable from the data; for group 2, although additional systematic perturbation is applied, the best fits still match the data very well. The input and best-fit torus models usually overlap each other closely, especially, at  $\sim 5 - 20 \mu\text{m}$ , where the torus component dominates the entire model. However, for some cases the input and best-fit torus models start to deviate at  $\lambda > 20 \mu\text{m}$ , mainly because the DL07 component starts to couple with the torus component. The large discreteness of the DL07 parameters makes the fitting challenging to find the true values (Shangguan et al. 2018). When comparing the input and best-fit parameters, we find that the exact input parameters are not easily reproduced in the fitting, likely because of the difficulty of distinguishing between subtle variations of the torus models, as well as the degeneracy between the torus and the DL07 model. The torus model is especially degenerate for the wind component, as templates generated from different configurations of model parameters produce only subtle differences in the resulting SEDs. Thus, caution should be exercised in interpreting the best-fit parameters of the torus model for individual objects, especially parameters associated with the wind component. In contrast to the uncertainties of the wind component, the integrated luminosity of the torus ( $L_{\text{torus}}$ ) can be recovered very reliably ( $\sim 0.02 - 0.03$  dex; Figure 16). The torus half-opening angle ( $\theta$ ) also suffers from no systematic bias, although the scatter is substantial ( $\sim 6^\circ - 7^\circ$ ; Figure 17). Thus, the overall statistical trend between  $\theta$  and  $\lambda_{\text{Edd}}$  (Figure 11) should be robust, even if the large observed scatter may be due to uncertainty in individual measurements.